

This is an Open Access document downloaded from ORCA, Cardiff University's institutional repository: <https://orca.cardiff.ac.uk/id/eprint/136914/>

This is the author's version of a work that was submitted to / accepted for publication.

Citation for final published version:

Chraiki, Ibtissam, Bouougri, El Hafid, Chi Fru, Ernest, Lazreq, Nezha, Youbi, Nasrddine, Boumehdi, Ahmed, Aubineau, Jérémie, Fontaine, Claude and El Albani, Abderrazak 2021. A 571 million-year-old alkaline volcanic lake photosynthesizing microbial community, the Anti-atlas, Morocco. *Geobiology* 19 (2), pp. 105-124. 10.1111/gbi.12425

Publishers page: <http://dx.doi.org/10.1111/gbi.12425>

Please note:

Changes made as a result of publishing processes such as copy-editing, formatting and page numbers may not be reflected in this version. For the definitive version of this publication, please refer to the published source. You are advised to consult the publisher's version if you wish to cite this paper.

This version is being made available in accordance with publisher policies. See <http://orca.cf.ac.uk/policies.html> for usage policies. Copyright and moral rights for publications made available in ORCA are retained by the copyright holders.



1 **Ibtissam Chraiki<sup>1</sup>, El Hafid Bouougri<sup>1</sup>, Ernest Chi Fru<sup>2</sup>, Nezha Lazreq<sup>1</sup>,**  
2 **NasrddineYoubi<sup>1,3,4</sup>, Ahmed Boumehdi<sup>1,3</sup>, Jérémie Aubineau<sup>5</sup>, Claude Fontaine<sup>5</sup>,**  
3 **Abderrazak El Albani<sup>5</sup>**

4

5 <sup>1</sup>Department of Geology, Faculty of Sciences-Semlalia, Cadi Ayyad University, Marrakesh,  
6 Morocco.

7 <sup>2</sup>College of Physical and Engineering Sciences, School of Earth and Ocean Sciences, Centre  
8 for Geobiology and Geochemistry, Cardiff University, Cardiff CF10 3AT, Wales, UK

9 <sup>3</sup>Instituto Dom Luiz, University of Lisbon, Portugal.

10 <sup>4</sup>Faculty of Geology and Geography, Tomsk State University, Tomsk, Russia

11 <sup>5</sup>University of Poitiers, CNRS IC2MP UMR 7285, Poitiers, France.

## 12 **Correspondence**

13 Abderrazak El Albani,

14 University of Poitiers, CNRS IC2MP UMR 7285, Poitiers, France

15 Email: [abder.albani@univ-poitiers.fr](mailto:abder.albani@univ-poitiers.fr)

16

17

18

19

20

21

22

23 **Abstract**

24 The Ediacaran period coincides with the emergence of ancestral animal lineages and  
25 cyanobacteria capable of thriving in nutrient deficient oceans which together with  
26 photosynthetic eukaryotic dominance, culminated in the rapid oxygenation of the Ediacaran  
27 atmosphere. However, ecological evidence for the colonization of the Ediacaran terrestrial  
28 biosphere by photosynthetic communities and their contribution to the oxygenation of the  
29 biosphere at this time is very sparse. Here, we expand the repertoire of Ediacaran habitable  
30 environments to a specific microbial community that thrived in an extreme alkaline volcanic  
31 lake 571 Myr ago in the Anti-atlas of Morocco. The microbial fabrics preserve evidence of  
32 primary growth structures, comprised of two main microbialitic units, with the lower section  
33 consisting of irregular and patchy thrombolitic mesoclots associated with composite  
34 microbialitic domes. Calcirudite interbeds, dominated by wave-rippled sandy calcarenites and  
35 stromatoclasts, fill the interdome troughs and seal the dome tops. A meter-thick epiclastic  
36 stromatolite bed grading upwards from a dominantly flat to wavy laminated base, transitions  
37 into low convex laminae consisting of decimeter to meter-thick dome-shaped stromatolitic  
38 columns, overlies the thrombolitic and composite microbialitic facies. Microbialitic beds  
39 constructed during periods of limited clastic input, and underlain by coarse-grained  
40 microbialite-derived clasts and by the wave-rippled calcarenites, suggest high-energy events  
41 associated with lake expansion. High-resolution microscopy revealed spherulitic aggregates  
42 and structures reminiscent of coccoidal microbial cell casts and mineralized extra-polymeric  
43 substances (EPS). The primary fabrics and multistage diagenetic features represented by active  
44 carbonate production, photosynthesizing microbial communities, photosynthetic gas bubbles,  
45 gas-escape structures, and tufted mats, suggest specialized oxygenic photosynthesizers thriving  
46 in alkaline volcanic lakes, contributed towards oxygen variability in the Ediacaran terrestrial  
47 biosphere.

48

49 **Keywords:** stromatolites; thrombolites; lacustrine, Ediacaran, oxygen; oxygenation

50

## 51 **Introduction**

52 Microbialites are lithified bio-sedimentary deposits formed through the trapping and binding of  
53 sediment grains by benthic microbial communities and/or in situ mineral precipitation and  
54 organomineralisation (Eymard, Alvarez, Bilmes, Vasconcelos, & Ariztegui 2020; Riding,  
55 1991). These biologically derived organo-sedimentary structures vary in shape, including  
56 columnar, sheet-like and domal structures, dependent upon the microbial community involved  
57 in their construction, the environment, physicochemical conditions, and the level of overlay.

58 Microbial deposits can be laminated or non-laminated, based on their framework. For example,  
59 stromatolites form laminated microbial deposits, while thrombolites, dendrolites and leiolites  
60 represent non-laminated microbialites, all displaying diverse shapes and fabrics (Noffke &  
61 Awramik, 2013; Riding, 2011). Laminated and lithified microbial deposits may preserve a  
62 variety of fine- and coarse-grained fabrics (Riding, 2011; Suarez-Gonzalez, Benito, Quijada,  
63 Mas, & Campos-Soto 2019). Fine-grained carbonate microbialites consist usually of alternating  
64 micrite and microsparite laminae that occasionally preserve calcified microbes that show up  
65 mainly as products of syngedimentary microbial precipitation. Clotted and peloidal fine-grained  
66 microfabrics are broadly similar to those produced by heterotrophic bacterial calcification of  
67 EPS and other cell products.

68 Moreover, it is widely accepted that cyanobacteria, together with whole community metabolic  
69 activity, are crucial to sedimentary carbonate production by precipitating and incorporating  
70 carbonate into the protective sheaths and EPS (Dupraz & Visscher, 2005; Altermann et al.,  
71 2006). Interactions between heterotrophic microorganisms and cyanobacteria communities are  
72 believed to have contributed significantly to carbonate biomineralization as far back as the late  
73 Archean (Bosak, Knoll, & Petroff 2013). The trapping of sand particles by uncalcified EPS and  
74 microbial filaments, including those produced by microalgae, construct coarse agglutinated

75 stromatolitic and thrombolitic deposits (Andres & Pamela Reid, 2006; Riding, 2011; Suarez-  
76 Gonzalez, Benito, Quijada, Mas, & Campos-Soto 2019). Since Archean time, microbial mats  
77 and microbialites are thought to have flourished in a wide variety of environments, ranging  
78 from marine to continental, and including hypersaline and volcanic alkaline lakes.

79 In the modern setting, great environmental diversification has enabled our understanding of the  
80 relationships existing between depositional setting, microbial remains, and extant communities  
81 as analogues of fossilized microbialites (Eymar et al, 2020). Present-day examples of alkaline  
82 lake microbialites include Shark Bay and Lee Stocking Island microbialites (Chagas, Webb,  
83 Burne, & Southam 2016; Kaźmierczak et al., 2011; Kremer, Kaźmierczak, & Kempe 2019).  
84 Our understanding of these modern and active microbial structures, together with their  
85 characteristic large carbonate and siliciclastic edifices have been used extensively in  
86 reconstructing the temporal and spatial distribution of early microbial communities.

87 Extreme physical and chemical conditions defined by the presence of  $\text{Na}^+$  as major cations,  
88 elevated  $\text{HCO}_3^-$  and  $\text{CO}_3^{2-}$ , and pH up to 9-12, promote the growth of microbial communities  
89 known as alkaliphiles in modern volcanic habitats and alkaline hot springs, where additional  
90 alkalinity is produced by the decomposition of silicate rocks (Hensel et al., 1997). These  
91 alkaline lake ecosystems are one of Earth's most productive and naturally occurring aquatic  
92 microbial mat habitats (Pecoraino & Alessandro, 2015), where alkaliphilic extremophiles  
93 survive by adapting to multiple environmental stressors, including permanently elevated  
94 alkalinity and temperatures (Schagerl & Burian, 2016). Biogeochemical co-evolution of water  
95 chemistry and microbial metabolic activities result in the abiotic and biotic precipitation of  
96 authigenic minerals as a solubility buffering mechanism, resulting in reprecipitated carbonate  
97 minerals, being the least soluble and first to precipitate (Sanz-Montero et al., 2019).

98 Here we present an example of an Ediacaran volcanic alkaline lake ecosystem characterized by  
99 a variety of well-preserved microbialite morphologies representing a unique and diverse  
100 community of alkaliphilic extremophiles that thrived in a caldera setting 571 Myr ago. We  
101 explore this unique late Neoproterozoic ecosystem and examine the associated biodiversity and  
102 biogeochemical developments that may have contributed to the dramatic Ediacaran  
103 biodiversification of life into complex oxygen-respiring ecosystems.

#### 104 **Geological setting**

105 The distinct Moroccan Anti-atlas sedimentary succession trending ENE–WSW, stretches from  
106 the shores of the Atlantic Ocean in West Africa, to the Tafilalt plain in southern Morocco  
107 (Figure 1a). The Eburnean Paleoproterozoic and Pan-African Neoproterozoic basement is  
108 unconformably overlain by an Upper Ediacaran and Paleozoic succession consisting of the thick  
109 volcanic and volcanoclastic Ouarzazate Supergroup (Thomas et al., 2002). The entire package  
110 is complicated by post-orogenic volcanic/volcaniclastic successions composed of subordinate  
111 clastic/epiclastic lithologies that unconformably overlie the Bleida and Sarhro Groups and post-  
112 structural granitoid sequences (Thomas et al., 2002). Most rocks in the Saghro inlier and the  
113 northernmost reaches of the Bou Azzer inlier, are comprised of Ediacaran volcanic rocks and  
114 clasts belonging to the Ouarzazate Supergroup associated with sub-volcanic plutons and dikes  
115 (Walsh et al., 2012). The Ouarzazate Supergroup was previously subdivided into lower  
116 volcanoclastic, volcanic and granitic lithologies labeled "XIII<sub>m</sub>", and an upper "XIII<sub>s</sub>" unit  
117 dominated by volcanoclastic and volcanic rocks isolated by an unconformity (Thomas, Fekkak,  
118 Ennih, Errami, & Loughlin 2004; Tuduri et al., 2018; Walsh et al., 2012). Most of the volcanic  
119 rocks are peraluminous to metaluminous, and range from andesitic basalts to rhyolitic  
120 lithologies with high-K calc-alkaline to shoshonitic affinities (Walsh et al., 2012). The  
121 structural, sedimentological, and volcanic features indicate subaerial effusive volcanic activity  
122 from several active centers containing calderas, and subaerial sedimentary sequences of

123 alluvial, fluvial and colluvial origin. The main known Caldera complexes in the central and  
124 eastern Anti-atlas are Achkoukchi in Sirwa, Oued Dar'a and Qal'at Mgouna in Jbel Saghro  
125 (Thomas et al., 2002; Tuduri et al., 2018; Walsh et al., 2012).

126 To the southeast of the Saghro massif (Figure 1a, b), the Ediacaran Oued Dar'a caldera in the  
127 lower Ouarzazate Supergroup consists of an enormous rectangular-shaped volcanic structure,  
128 11 km wide and 18 km long. The caldera, situated along a northeast corridor, is composed of  
129 an incredibly well preserved infill made up of trachytic, trachydacitic and rhyolitic ash-flow  
130 tuffs ponded within a large volcano (Walsh et al., 2012). The northeast margin is intruded by  
131 pink granite interpreted as parent magma of the volcanic rocks (Figure 1b). The southwestern  
132 margin (Choubert and Faure-Muret, 1970) is marked by a 200 m coarse-grained, quartz-rich,  
133 and granulated volcanoclastic deposit resting on the caldera's infill ash-flow tuff that is  
134 intercalated with lacustrine beds containing purplish-green microbialites (Álvaro et al., 2010;  
135 Walsh et al., 2012; Álvaro & González-Acebrón, 2019). The age of the caldera infill has been  
136 estimated to the last major volcanic eruption from the caldera  $\sim 571 \pm 5$  Ma according to Walsh  
137 et al., 2012 (Figure 1b).

138 This study is focused on the Amane Tazgart carbonates located on the western edge of the  
139 Saghro inlier (Figure 1b, c), located  $\sim 25$  km southeast of the Ouarzazate classical geological  
140 fieldtrip stop along the Ouarzazate–Zagora Agdz road (*e.g.*, Choubert & Faure-Muret, 1970).  
141 Choubert and Faure-Muret (1970) were the first to propose a lacustrine depositional setting for  
142 these meter-thick, carbonate-bearing volcano-sedimentary units, in view of their restricted  
143 geographic expansion and the obvious nearness of domal and conical stromatolites. The  
144 development of the Amane Tazgart microbialites was controlled primarily by the caldera's  
145 volcanic and geothermal activity, combined with silicate hydrolysis under subtropical  
146 conditions (Álvaro et al., 2010; Álvaro & González-Acebrón, 2019).

## 147 **Materials and Methods**

148 Field mapping, logging, sampling and facies analysis were conducted during two field trips  
149 involving two sections and 49 samples. Thin sections were produced for detailed petrographic  
150 observations with a ZEISS Discovery V8 microscope equipped with an AxioCam ERc 5s  
151 camera at the University of Poitiers. Mineralogical composition was investigated by X-ray  
152 diffraction (XRD) on a subset of 25 representative agate mortar powdered samples. The samples  
153 were analyzed with an Xpert Pro Bragg/Bentano diffractometer at the University of Poitiers  
154 using CuK $\alpha$  radiation operating conditions of 40 kV and 40 mA. Powdered samples were  
155 analyzed at the 2 to 65° 2 $\theta$  angular range, using 0,017° 2 $\theta$  step sizes per 0,7 s. After air drying,  
156 ethylene glycol solvation, and heating at 350°C and 550°C, the clay fraction was analyzed over  
157 an angular range of 2–35° 2 $\theta$  at 0,017° 2 $\theta$  using 0,7 s step sizes. Mineralogical identification  
158 was performed using the Xpert High-score pro software by comparing the data to the  
159 International Centre for Diffraction Data (ICDD) database (*e.g.*, Moore & Reynolds, 1997).

160 A sample from each facies type was hand-crushed to 1-5 particle cm size and dissolved in 10%  
161 diluted acetic acid for 8 to 24 hours, for microfossil analysis. Suspected microfossil remains  
162 were picked out from the acid residues using a stereoscopic microscope and then imaged at  
163 high resolution with scanning electron microscope EDAX-AMETEK SPEC\_007 at Cadi Ayyad  
164 University, Morocco and with JEOL JSM IT 500 at Poitiers University, France.

## 165 **The Ediacaran Amane Tazgart microbialites**

### 166 *General description*

167 The Amane Tazgart succession forms a lens-shaped unit, is less than 1 km wide and up to ~15  
168 m thick in the central part (Figure 1c). The succession is less folded, slightly dipping WNW  
169 and divided by a NNE-SSW fault into two compartments (Figure 1d). It is underlain by grey  
170 aphanitic andesitic magmas and overlain by a volcano-sedimentary succession including

171 andesitic lava flows, peperites and epiclastic micro-conglomerates and sandstones rich in  
172 volcanic clasts. The surrounding depositional setting dominated by subaerial volcanic and  
173 sedimentary setting of the Oued Dar'a Caldera, as well as the overall facies features of the  
174 Amane Tazgart, suggest short periods of attenuated volcanic activity that are accompanied by  
175 lacustrine sediment deposition in ephemeral ponds (*e.g.*, Álvaro et al., 2010; Álvaro &  
176 González-Acebrón, 2019)

177 The lower boundary of this succession is erosional and locally preserves lens-shaped  
178 conglomerates and narrow trough fillings (Figure. 1c). The investigated clastic and carbonate  
179 layers overlying the conglomerates along the whole area of Amane Tazgart show lower and  
180 upper packages preserving diverse varieties of microbialites and associated non-microbialitic  
181 deposits (Figure 2). The lower part consists of four sequences, decimeter to meter thick, each  
182 ending with beds of microbialites numbered in the measured section as H1 to H4. In general,  
183 the first sequence starts with irregular patchy clotted thrombolites and stromatolites (Figure 2),  
184 overlain by thick pale cream bioherme layers that coalesce to form the wide H1 domes. The  
185 H2-H4 microbialitic layers in the overlying sequences are preceded by clastic carbonates  
186 containing rippled sandy calcarenites, cross-bedded, and graded calcirudites dominated by  
187 clast-derived microbialites, and cm-thick interbeds of fine-grained laminated sandstones and  
188 siltstones. Within the microbialitic and non-microbialitic deposits, carbonate spherulitic grains  
189 occur in both the clastic and carbonate lithologies. The Upper section forms a widespread  
190 meter-thick layer along the Amane trough and consist of planar laminated and rippled medium  
191 to fine-grained epiclastic sandstones and siltstones dominated layer. These are overlain by the  
192 last microbialitic horizon H5 that preserve vertically trending stromatolites and laminations  
193 buried by peperites and the overlying volcano-sedimentary rocks.

#### 194 **Amane Tazgart microbialites: morphotypes and fabrics**

195 ***Patchy thrombolites and microstructures***

196 The lithological features of the Amane Tazgart microbialites, distinguish thrombolitic,  
197 stromatolitic, and composite microbialites made largely of domal carbonaceous and clastic  
198 stromatolites (Figure 2).

199 The thrombolitic microbialites are built on a framework characterized predominantly by  
200 mesoclots, matrix cement, and voids. One type of mesoclots appears frequently in the sampled  
201 sections, being commonly irregular to patchy in shape (Figure 3a, b). A matrix composed of  
202 fine-grained epiclastic sediments filled the spaces between the mesoclots, and appears reddish  
203 to purplish on fresh and polished surfaces (Figures 3a, b). The thrombolitic voids are usually  
204 filled with light sparitic cement that is locally replaced by late diagenetic microcrystalline  
205 quartz.

206 Microscopically, the mesoclots are characterized by clotted to peloidal micrite, with some  
207 scattered sand- to silt-sized clastic grains of quartz, feldspar and iron-impregnated volcanic  
208 composition. The mesoclots are surrounded by fan-shaped to botryoidal calcite cement (Figure  
209 3c). Occasionally, mesoclots preserve faint relatively thin laminations, which consist of  
210 alternating sparitic and clotted micritic laminae (Figure 3d). The matrix is mainly epiclastic,  
211 and partially silicified. In some cases, sediments between the mesoclots contain distinctive  
212 wavy and wrinkly laminations expressed as wrinkly-crinkly dark clastic grain-trapping laminae  
213 (Figure 3e).

214 ***Composite domal microbialites***

215 Composite microbial structures between the thrombolites and stromatolites are common  
216 (Figure 3f), making up the principal structure of horizons H1 and H3. The composite framework  
217 within each dome can be observed at distinct scales, with the stromatolitic fabric dominating in  
218 many domes whereas the thrombolitic forms are isolated in small domes at the base and/or in

219 the patchy and irregular layers that are draped and encrusted by stromatolites (Figure 3f, g, h).  
220 Centimetric non-branched columns were identified intermingling with the patchy clots, while  
221 the microstructural fabric holding the thrombotic mesoclots together, preserve typical clotted  
222 to peloidal micrite. Thin laminated stromatolites and occasional peloids fill the inter-mesoclots  
223 spaces (Figure. 3h). The dominating laminated fabrics in these domes display grain-sized,  
224 micritic fine-grained, and sparitic laminae. The grain-sized laminae preserve wrinkled features  
225 and form lens-shaped layers with quartz, feldspar and volcanic clasts embedded in a partly  
226 silicified amorphous matrix (Figure 3i). The micritic finer and dark laminae, may contain sparse  
227 and fewer finer clastic grains, are continuous, sometimes lenticular, and characterized by a  
228 dense fabric. The sparitic laminae are the lightest in color and constituted of well-crystalized  
229 abiogenic sparry layers (Figure 3f).

### 230 *Flat large domal stromatolites*

231 This morphotype occurs along two beds and are up to 30 cm thick, within the microbialitic H2  
232 and H4 horizons (Figure 2). At the field scale, they correspond to flat and large laterally linked  
233 stromatolitic domes of up to 1 m in diameter (Figure 3j). Internal laminations are very fine,  
234 showing regular and typical wavy and crinkly features (Figure 3k), consisting of alternating  
235 dark micritic to microsparitic light laminae, grainy calcitic laminae and iron crusts enhanced by  
236 tufted microbial mats. Tufts form vertically oriented cone shaped laminae induced by the  
237 growth of the filamentous microbial communities (Gerdes, 2010; Gerdes, Klenke, & Noffke  
238 2000). They are typically 0.02 cm in height but can grow to 0.1 cm (Figure 3l), and are internally  
239 filled with fine to medium-grained sediment and macro-sparitic calcite.

### 240 *Clastic dominated stromatolites: morphotypes and microstructures*

241 The clastic dominated stromatolites appear in microbialitic horizon H5. They form a single bed  
242 up to 2 m in thickness, and preserve a succession of four morphotypes ranging from flats to  
243 crinkly laminated domes, cones, and laterally linked hemispheroidal columns. The flat to

244 crinkly laminated framework consisting of sub-millimeter lamination appears in the lower parts  
245 of the stromatolitic bed (Figure 2). In the upper section, the planar laminated stromatolites  
246 occupy the interdome troughs, forming layers of up to 10 cm thick which grade vertically into  
247 small domes of up to 5 cm in diameter (Figure 4a). Domes up to 0.5 m high (Figure 4b) and 30  
248 cm wide, together with conical morphotypes reaching heights of 0.1 m and varying widths of  
249 0.1-0.2 m (Figure 4c), occupy the upper thick portions of horizon H5. The last morphotype  
250 consists of laterally linked hemispheroidal structures, which overlay the flat laminated  
251 stromatolites. The hemispheroidal features appear spaced on bedding surfaces and preserve  
252 subcircular to elliptical sections with diameters ranging from 5 to 8 cm (Figure 4d, e). The  
253 vertical section shows inclined to elongated hemispheroids with a NW-SE general trend similar  
254 to that of the wave ripples in the underlying clastic rocks. The propagation and scattering of big  
255 composite domes composed of laminations with circular axial column patterns that transition  
256 to a wavy architecture at the margins, suggest strong competition for space and growth (Figure  
257 4f). The various stromatolitic structures grew inside large metric domes or biostromes, of a  
258 thickness varying between 1-1.2 m, while the flat-laminated to pseudo-columnar stromatolites  
259 that developed in the interdome spaces, tend to alternate with red epiclastic sands that filled the  
260 interdome spaces.

261 In thin section, the biolaminations in the clastic stromatolites consist of alternating medium  
262 sand-sized to silt-sized clastic, micritic, iron-stained and sparitic laminae. The grainy laminae  
263 forming the main component of these stromatolites (Figure 4g) preserve a wavy and wrinkled-  
264 crinkled fabric, formed by medium to coarse-grained epiclastic grains and tuffs with lots of  
265 feldspar derived from the surrounding volcanic rocks, including iron, rock fragments, and clay  
266 minerals. The micritic laminae are represented by a dense fabric composed of scarce oxides,  
267 feldspar and peloidal laminae (Figure 4h, i). The color of micrite varies from brown to brownish  
268 red depending on the proportion of iron and clay minerals, where increasing iron enrichment

269 and clay content are associated with a darker coloration (Figure 4h, i), with the iron-rich layers  
270 being the darkest (Figure 4g). These iron-rich layers consist of thin laminae that are less than 1  
271 mm thick, composed of iron and volcanic grains and sometimes represent the main crusts  
272 between the clastic rich laminae. The sparitic laminae correspond to well crystalized,  
273 essentially, abiogenic sparry layers (Figure 4h).

274 Noticeable, are almost perfectly rounded features encased by contorted dark laminae, identified  
275 in the flat domal and conical stromatolites. Most of these features ranging in size from 3-100  
276  $\mu\text{m}$  are partially filled by diagenetic microcrystalline quartz (Figure 4j). Other features  
277 supporting gas production beneath the mats are vertically oriented ptygmatic veins cutting the  
278 biolaminations, interpreted as gas-escape structures. These laminations are arranged into layers  
279 corresponding to those defined by Monty (1976) as repetitive and alternating, with most  
280 belonging to the composite alternate type (Figure 4k). The grain-sized sparitic or micritic and  
281 sparitic laminae form the frequently observed alternating laminations (Figure 4h, k). On the  
282 other hand, the light sparitic layers containing thin peloidal micritic laminations and sparite are  
283 associated with composite-style laminations, while micritic/organic crusts separate repetitive  
284 laminations in the grain-sized beds (Figure 4l).

## 285 **Non microbialitic deposits**

### 286 *Calcirudites with microbialite-derived clasts*

287 Several lens-shaped coarse-grained layers of poorly sorted microbialitic clasts are interbedded  
288 with the microbialitic deposits, and contain clasts ranging in size from 0.3-2 cm. The shapes of  
289 the clasts distinguish subrounded and flat-pebble dominated calcirudites clasts (Figure 5a-b).  
290 The flat-pebble rich calcirudites suggest on-site deposition and weak reworking of lithified  
291 microbialites, while the subrounded microbial clasts indicate strong reworking by wave induced  
292 currents. These sediments are interrupted and intermingled with centimeter-thick stromatolitic

293 laminations interpreted as representing conditions suitable for microbialite development being  
294 frequently interrupted by energetic currents.

295 Polished slabs show that most of the microbialitic clasts still preserve their primary features  
296 with clotted or laminated fabrics, some of them being partially or fully replaced by white  
297 diagenetic calcite (Figure 5a, b). The matrix consists of sand to silt-sized epiclastic sediments  
298 embedded in a microsparitic cement, and mostly derived from the reworking of the surrounding  
299 andesitic rocks (Figure 5a, b). Microscopically, the stromatoclasts alternate in composition  
300 from dark peloidal and clotted micritic to light microsparitic laminae. Medium coarse-grained  
301 epiclastic sediments cemented with microcrystalline quartz, occupy the spaces between the  
302 stromatoclasts, while sparitic calcite fills the remaining voids.

### 303 *Spherulites and spherulitic fabric.*

304 Red facies composed of fine to coarse-grained sandstones, full of spherulites, and poorly sorted  
305 microbialitic clasts (Figure 5c), occur in the basal part of the thrombolitic and composite  
306 microbialitic layers. Being spherical to oval, and ranging from 1 to 5 mm in diameter, the  
307 spherulites commonly develop into masses of deviated structures (Figure 5c). In thin section,  
308 the spherulite grains comprise fibro-radial and fan-shaped calcite crystals coating the nuclei  
309 that are generally darker than the cortex. These nuclei are composed mainly of micrite-  
310 microsparite cement and sometimes mixed with clastic elements similar to those of the  
311 surrounding matrix (Figure 5d).

### 312 *Rippled and parallel laminated sandy calcarenites*

313 These deposits occur within the microbialitic carbonates, with beds attaining heights of 30 cm.  
314 Internal structures consist of superposed sets of current and climbing ripple laminations.  
315 Occasionally, centimeter-thick stromatolitic laminations occur on top of the beddings planes,  
316 indicating limited microbial mat growth during low energy conditions (Figure 5e). The

317 stromatolitic layer preserves sub-millimetric wrinkly and crinkly laminations that alternate with  
318 coarse/fine-grained micritic laminae occasionally stained with iron (Figure 5f).

### 319 *Clastic sediments*

320 A sedimentary package of alternating rippled and parallel laminated epiclastic sands and shales,  
321 separates the carbonate and clastic units. These deposits display sedimentary features including  
322 ripple marks, crescent and mat-related structures (Banerjee et al., 2010). The ripple marks  
323 (Figure 6a) tend to change direction from layer to layer, suggestive of persistent turbulence.  
324 The MRS exhibits a wide range of surface morphologies related to mat-growth, mat-induced,  
325 and mat-protected structures (e.g., Riding, 2011). The Amane Tazgart MRS features exhibit  
326 domal sand buildups or stromatolitic sandy bedding surfaces on the sandstones (Figure 6b) with  
327 varying sizes. Grouped and ungrouped structures, which may occur on the same sandstone  
328 bedding surfaces, are protected in curved hyporelief on the soles of the overlying sandstone  
329 beds (Bottjer & Hagadorn, 2007). The crescent-shaped morphologies identified on the bedding  
330 surface of one sandstone bed (Figure 6c), show vertically oriented fluid escape structures filled  
331 with gas bubbles that impart a domal to conical shape to the superposed laminae (Figure 6d).

### 332 *Peperites*

333 The clastic stromatolitic domes are covered by peperites intermixed and intermingled with  
334 unconsolidated sediment and magma, considered as good evidence for unconsolidated and poorly  
335 consolidated wet sediments (e.g., Skilling, White, & McPhie 2002). These peperites are further  
336 linked to epiclastic sediments that are displaced by and trapped in lava flow (Figure 6e, f), including  
337 decimeter-thick globular andesitic lavas that are characterized by the upwards formation of  
338 elongated centimeter to decimeter sized clasts with increasing lava compositions (Figure 6e).

### 339 **Mineralogy**

340 The bulk mineralogy of the studied sections is predominated by calcite, quartz, plagioclase, and  
341 occasional illite and hematite (Figure 7). Detrital particles are present in all the microbialites  
342 and detrital facies, including K-feldspar, plagioclase, and hematite. We observe that the  
343 mineralogical composition of both the Amane Tazgart sections has changed since deposition  
344 first took place. In the lower sections (Figure 7a, b), calcite is predominant over quartz, in both  
345 the microbialitic (Figure 7a) and the non-microbialitic facies (Figure 7b), while the opposite  
346 occurs in the upper sections (Figure 7c, d). Clay mineralogy shows that illite and/or mica and  
347 chlorite are predominant (Figure 7). However, the mineralogical evolution through these two  
348 phases is unclear as indicated by the weak 001 reflection intensities. The <2  $\mu\text{m}$  clay size  
349 fractions show a predominance of chlorite, mica/illite, and chlorite/smectite (C/S) mixed-layer  
350 minerals (MLM) (Figure 8). This is dominated by chlorite and a fairly low degree of bulk  
351 organization at the base of the section in both, the microbialitic and the non-microbialitic layers,  
352 as indicated by a 15 Å peak in the ethylene-glycol treatments and a superlattice reflection of  
353 25-30 Å (Figure 8a, b). Upward, the MLM is increasingly enriched in smectite, with bulk  
354 organization of the C/S ratios shown by superlattice reflections of 29-30Å (Figure 8c- d).

### 355 **Biogeochemical reconstruction**

356 Following acetic acid dissolution of carbonates, several aggregates picked out and thoroughly  
357 examined by SEM-EDS, resulted in the identification of spherical, globular and irregular  
358 morphologies (Figure 9) similar to those described in modern microbial aggregates (Xiao, Li,  
359 & Reynolds 2018). Although only minor in occurrence, the elongated shapes are prevalent  
360 while the aggregates are mainly found associated with the spherulitic samples and occasionally  
361 within the thrombolites. Several aggregations are joined together by smooth mucus-like  
362 structures that sometimes drape the aggregates (Figure 10a-c). EDS analysis of the non-coated  
363 aggregates, reveal silica and a significant proportion of carbon (Figure 10d Spot 1), while the  
364 smooth mucus-like structures are composed mainly of carbon and sulfur, with a proportion of

365 silica, magnesium, arsenic and chlorine (Figure 10d-Spot 2). High-resolution SEM  
366 observations show the presence of globule-like and coccobacilli-like crystals, which resemble  
367 the remains of coccoidal and coccobacilli-like cyanobacteria. They occur within EPS-like  
368 material, display a size range of 1-2  $\mu\text{m}$ , and have affinities similar to those described  
369 by Chafetz, Barth, Cook, Guo, & Zhou (2018). These crystal structures preserved in silica  
370 contain a significant proportion of carbon and sulfur (Figures. 11a, Spot 1, Spot 2).

371 A representative sample from each facies, studied for ultrastructural characterization of the  
372 microbialites, and SEM examination of the thrombolitic samples, revealed numerous  
373 micropores mainly embedded in the calcitic crystals, indicative of potential bacterial molds  
374 (Figure 11b) and consistent with a microbial size range of 0.5-2  $\mu\text{m}$  (Tang, Shi, & Jiang, 2013).  
375 Although not unique to any known microbial morphotype, our observations are coherent with  
376 Proterozoic micritic and peloidal limestone facies, and when compared to modern analogues,  
377 their deposition has been strongly linked to the activity of cyanobacteria, with coccoidal forms  
378 represented by cell casts (Dongjie et al., 2013, Tang, Shi, & Jiang, 2013).

379 EDS analysis of the dark stromatolitic laminae, revealed clay minerals superimposed on each  
380 other, with no significant differences observed between the stromatolitic and thrombolitic facies  
381 (Figure 11c). The calcitic zones are always composed of micropores, and dark clayey  
382 laminations. Three-dimensional analyses of the spherulitic samples show calcitic wedges with  
383 rounded micritic nuclei representing chemical compositions different from the cortices. The  
384 cortices are composed of pure calcite ( $\text{CaCO}_3$ ), while the nuclei are composed of calcite  
385 associated with clays represented by Si, Al, K and iron, which explain the darker light  
386 attenuated composition of the nuclei in thin section (Figure 11).

## 387 **Discussion**

388 *Environmental controls on the genesis of the microbialites*

389 The harsh living conditions of alkaline volcanic lakes push organisms towards extreme  
390 physiological adaptations that enable and enhance the survival of specialized alkaliphilic  
391 populations. These microorganisms innovate resilient intra-cellular metabolic processes to  
392 overcome external physico-chemical stressors like high turbidity, dramatic increases in pH,  
393 elevated concentrations of toxic trace elements and metals, and the dramatic effects of  
394 extremely high temperatures on cell homeostasis, physiology and function (Schagerl & Burian,  
395 2016). Studies on modern alkaline lake ecosystems, demonstrate that microbes handle these  
396 persistent extreme environmental conditions through regulatory, conformity and avoidance  
397 processes (Willmer et al., 2004). The Amane Tazgart microbialites give new insights to the  
398 existence of successful and high productive terrestrial volcanic ecosystems during the Late  
399 Neoproterozoic that would have actively contributed towards the transformation of the  
400 Ediacaran biosphere, by for example, through oxygen and organic matter production.

401 The facies described in the Amane Tazgart succession, as well as the overall geodynamic  
402 setting, point to a terrestrial lacustrine setting with active microbial communities that played a  
403 crucial role in local biogeochemical cycles and redox. The microbialitic successions are encased  
404 in a volcanic complex exhibiting evidence of subaqueous explosive and effusive volcanic  
405 activities. Additionally, the sedimentary and volcano-sedimentary features indicate deposition  
406 in an alluvial and colluvial environment (Álvaro et al., 2010; Tuduri et al., 2018; Walsh et al.,  
407 2012). The microbialitic and non-microbialitic features, together with the vertical arrangement  
408 of the facies, indicate low-energy lacustrine conditions punctuated by high-energy events. The  
409 high-energy stages are associated with erosive currents producing mainly coarse-grained clastic  
410 carbonates dominated by ripped-up microbialitic clasts and wave-generated currents associated  
411 with cross-bedded calcarenites, planar laminated and wave-rippled sandstones. The low-energy  
412 conditions favored lake floor colonization by microbial mats, to produce at the incipient stages

413 patchy and irregular thrombolites and stromatolites overlain by large and coalescent dome-  
414 forming bioherms. The microfabric in the microbialitic carbonates and clastic stromatolites  
415 indicate the trapping and binding of sediments during critical intervals of low clastic input into  
416 the lake, suggesting that microbial oases flourished in the lake during short periods coincident  
417 with attenuated volcanic activity. The demise of this lake system and its microbial community  
418 occurred during an andesitic lava flow event, indicated by the peperitic facies blanket associated  
419 with horizon H5. These andesitic lavas provide a maximum age of  $571 \pm 5$  Ma, which is the  
420 age of the last major volcanic eruption from the caldera (Walsh et al., 2012).

#### 421 *Microbialite growth morphologies and environmental implication*

422 The subdivision of the Amane Tazgart section into a lower microbialitic and clastic carbonates,  
423 and an upper of clastic stromatolites and sandstone sections, separated by a meter-thick clastic  
424 layer composed of sandstones, and overlain by clastic stromatolites, is interpreted to imply  
425 significant chemical change and clastic sediment supply to the lake. This transition may be  
426 related to water depth fluctuations and calcium carbonate saturation. The vertical facies trends  
427 along the succession show sequences starting with shallow high-energy littoral deposits, and  
428 grading upwards into microbialites growing in quite-energy conditions. Such sequences, as well  
429 as the caldera setting, indicate limited water supply from runoff and active streams generally  
430 lacking in caldera ecosystems. In modern calderas and crater lake locations, water level  
431 fluctuations are mainly influenced by groundwater supply, hydrothermal springs, evaporation,  
432 and water supply to evaporation rate ratios (*e.g.* Pecoraino & Alessandro, 2015). Calcium  
433 carbonate saturation decreases from bottom to the top of the succession as indicated by the  
434 transition from calcite-dominated to quartz-dominated deposits (Figure 2). The shift in facies  
435 composition from carbonate-dominated to clastic-dominated fabrics, appears to be related to  
436 hydrological regime changes influenced by surficial water supply. It is also possible, and as  
437 demonstrated in modern situations, that some parameters like alkalinity, water temperature and

438 biological processes may have controlled carbonate saturation and precipitation (*e.g.*, Kremer,  
439 Kaźmierczak, & Kempe 2019) .

440 The association of clotted and laminated textures in the composite microbialites, imply  
441 variation of growth styles in the same environment, and suggests a complex transaction between  
442 processes favoring thrombolitic and stromatolitic textures that cannot be explained by simple  
443 changes in environmental conditions (Harwood & Sumner, 2011). On the other hand, the  
444 relative proportion, distribution and upward increase of stromatolitic fabrics at the expense of  
445 the thrombolitic communities, can be attributed to local environmental variations within the  
446 same broad environment. Thus, this co-occurrence of clotted and laminated fabric may suggest  
447 that the different textures are the result of simultaneous growth of morphologically distinct  
448 microbial communities (Harwood & Sumner, 2011), and that stromatolitic communities  
449 became more dominant with the age and the chemical evolution of the lake, and became the  
450 last community to finalize the construction of the epiclastic stromatolitic horizon.

451 Upon appearance, the stromatolitic features in the clastic horizon produce flat shallow water  
452 morphologies, which we link to frequent sediment supply, sediment composition, and grain size  
453 distribution (Andres & Reid, 2006). The change from flat to columnar stromatolitic  
454 morphotypes has previously been considered to indicate an upward deepening sequence  
455 associated with occasional sand burial which leads to the development of columns (Andres &  
456 Reid, 2006). However, the change from columnar to domal stromatolitic forms has also been  
457 related to a deepening event (Adachi et al., 2019), while progression from columnar to dome-  
458 shaped stromatolitic environments was further interpreted as a feature of sediment flux rates  
459 (*e.g.*, Planavsky & Grey, 2008). Consequently, the enrichment of detrital materials in the  
460 columnar and dome-shaped morphotypes, implicate the influence of sediment flux rates on the  
461 development of the stromatolitic morphologies. Vertical column diameter changes, reflect  
462 microbial activity, following small-scale environmental fluctuations. When microbial activity

463 weakens, the upward growth of stromatolites is compensated by a decrease in diameter (Adachi  
464 et al., 2019). Furthermore, bridges develop between cyanobacterial columns and domes when  
465 microbial activity intensifies in abundant sunlight to generate sufficient photosynthetic energy  
466 to enable the extension of mats across the individual columns and the sediment-filled cavities  
467 between them (Adachi et al., 2019).

468 The presence of C/S and MLM clays minerals in the microbialitic and non-microbialitic facies,  
469 is a feature of hypersaline environments, hydrothermally altered basalts and ultrabasic rocks,  
470 burial diagenesis of volcanoclastics, graywackes, and contact metamorphism (Środoń, 1999  
471 and references therein). In our case, there was no petrographic evidence for metamorphic  
472 alteration. Therefore, the presence of C/S MLM in all the facies is most parsimoniously  
473 interpreted as related to the hyper salinity of the lake, and/ or to burial diagenesis.

474 The revelation of smooth mucus like structures, their shape and composition, point to a likely  
475 EPS provenance, similar to those reported in Mesoproterozoic thrombolites from China  
476 (Dongjie et al., 2013). They share many similarities in terms of size and morphology, with  
477 mineralizing EPS reported in hypersaline microbial mats from Qatar (Perri et al., 2018). The  
478 Ca, Si, Al, S and Mg concentrated in the EPS-like remains, typically contribute to EPS  
479 mineralization and preservation in sediments (Perri et al., 2018). Similarly, potential As  
480 enrichment by EPS has been associated with Archean and Proterozoic microbialites (Sforna et  
481 al., 2017; Aubineau et al., 2019), as in our samples and EPS from modern microbial  
482 communities living in hypersaline lakes associated with photosynthesis and volcanic activity  
483 (Sforna et al., 2017; Sancho-Tomás et al., 2018).

484 Spherulites are composed mainly of calcite crystals and are associated with thrombolitic and  
485 composite microbialites, where the main mineralogical phase is carbonate, which is necessary

486 for the development of spherulites. In epiclastic stromatolites, the main mineralogical phase is  
487 quartz, with only traces of carbonate minerals, which may explain their lack of spherulites.  
488 Spherulites formation was previously related to microbial activity, through association with the  
489 presence of EPS which generated favorable microenvironments for calcium carbonate  
490 precipitation at the sediment–water interface, or just beneath the sediment-water interface (e.g.,  
491 Kirkham & Tucker, 2018; Mercedes-Martín et al., 2016). Further, Mercedes-Martín et al.  
492 (2016) revealed typical spherulitic-radial calcite developing in saline alkaline water and in the  
493 presence of specific dissolved organic acids, which are strong constituents of EPS.  
494 Nevertheless, an abiotic origin for spherulites has been related to changes in lake chemistry,  
495 including temperature, pH, and Si, Mg and Ca fluxes (Wright & Barnett, 2015). Abiotic  
496 formation of spherulites inside a suspension of poorly crystalline Mg-Si gels has been reported  
497 in soda lakes when long-term evaporative water loss builds sufficient dissolved Si and Mg to  
498 elevate Mg-Si gel precipitation (Wright & Barnett, 2015). However, our case lacks evidence in  
499 support of the predominance of Mg-Si mineral phases. Instead, extracellular polymeric  
500 substances are associated with the spherulitic, as well as the thrombolitic and composite  
501 microbialitic assemblages. Taken together, the highlighted necessity of EPS in the precipitation  
502 of spherulites, EPS elemental properties, and occurrence in analogue modern environments  
503 similar to our Ediacaran setting, strongly support the biogenic origin of the mats. Importantly,  
504 EPS is a major factor in the formation of microbial aggregates and crucial for maintaining the  
505 three-dimensional structure of microbial biofilms (Sheng, Yu, & Li 2010).

506 The gas-bubble sizes in the Amane Tazgart microbialites, and their near-perfectly round shape,  
507 is consistent with those depicted in modern and ancient mat-related structures and stromatolites  
508 (Aubineau et al., 2019; Bosak et al., 2009; Sallstedt, Bengtson, Broman, Crill, & Canfield  
509 2018). Tufted structures and gas-bubbles are commonly tied to high oxygenic photosynthetic  
510 activity, generated by cyanobacteria, interpreted to indicate sufficient gas accumulation to

511 overcome considerable hydrostatic pressure at depth (Bosak, Liang, Min, & Petroff 2009,  
512 Bosak et al., 2010). Furthermore, experiments with laboratory-grown cyanobacterial mats  
513 suggest that both mat-trapped and mat-attached bubbles are saturated with O<sub>2</sub> compared to the  
514 overlaying atmosphere. Hence gas bubbles in sedimentary rocks are primarily interpreted as  
515 remnants of oxygenic photosynthetic activity against non-photosynthetic gases (Bosak et al.,  
516 2010). A study of Antarctic microbial mats from Lake Fryxell, report cyanobacteria developing  
517 O<sub>2</sub> oases in benthic microbial mats, even at very low net photosynthetic rates of 0.05 μmol O<sub>2</sub>  
518 m<sup>-2</sup>s<sup>-1</sup> at 9.8 m (Sumner, Hawes, Mackey, Jungblut, & Doran 2015). By implication, the  
519 abundant bubbles in our mats suggest high oxygenic photosynthetic rates likely dominated by  
520 alkaliphilic cyanobacteria, pointing to environmental radiation and habit specialization in the  
521 cyanobacteria by the Ediacaran time.

522 Further, the data hint that extreme alkaline lake environments like those of the photosynthetic  
523 mono lakes of California where volcanic arsenic fuels anoxygenic photosynthesis (Kulp et al.,  
524 2008; McCann et al., 2016), may have been a common feature of the Ediacaran biosphere.  
525 Intriguingly, As is associated with our EPS material, with elevated levels proposed for the  
526 Ediacaran biosphere (Chi Fru et al., 2015), where strong resilience to As detoxification would  
527 have been a key requirement for survival (Chi Fru et al., 2018).

### 528 *Microbialites and diagenesis*

529 Álvaro & González-Acebrón (2019) have characterized a number of diagenetic aspects in the  
530 Amane Tazgart microbialites similar to other sections of the Anti-atlas. They described several  
531 early-diagenetic processes, punctuated by polyphasic fissuring related to hydrothermal activity,  
532 with the generation of fibrous, botryoidal and blocky/drusy mosaic calcites, idiotopic mosaics  
533 of dolomite, and euhedral to drusy calcite produced by dedolomitization. They recognized  
534 silicification as early diagenetic occlusion of sediment/water interface interparticle porewater  
535 spaces within a pyroclastic rock setting, and hydrothermal silica precipitation in secondary

536 pores (Álvaro & González-Acebrón, 2019), consistent with our observations. We note that  
537 intraparticle pores in the carbonate units were filled mainly by sparite, unlike those in the clastic  
538 stromatolites that are filled by early diagenetic microcrystalline quartz. This observation  
539 provides support for an initial carbonate-rich water column that subsequently developed to  
540 enrich silica at the expense of calcite. The carbonate armor of the first microbialitic unit makes  
541 them unstable and strongly vulnerable to diagenetic processes and hydrothermal activity. On  
542 the other hand, the clastic stromatolites confer more resistance, indicated by their restriction to  
543 early diagenetic silicification and hydrothermal silicification.

544

## 545 **Conclusions**

546 The Amane Tazgart succession provides an example of early cyanobacteria radiation and  
547 habitat specialization. Several modern examples in similar “volcanic lake” settings are well  
548 studied and host mainly extremophilic microbial communities specialized to extreme  
549 environmental conditions, which include among others, elevated alkalinity, salinity and  
550 temperatures (Merino et al., 2019; Pecoraino & Alessandro, 2015). It was not until towards the  
551 end of the Ediacaran that some of the most rudimentary forms of complex animals first  
552 appeared, implying a bulk of Earth’s history has been dominated by microbial life, stretching  
553 back to the Archean (*e.g.*, Knoll, Bergmann, & Strauss 2016; Van Kranendonk et al., 2019).  
554 Remnants of Archean life have been described from volcanic settings as microbially related  
555 deposits and structures preserving evidence for their biogenicity (Hickman, Cavalazzi, Foucher,  
556 & Westall 2018; Stüeken & Buick, 2018; Van Kranendonk et al., 2019). The Amane Tazgart  
557 succession highlights an exceptional Ediacaran case predating the Cambrian explosion,  
558 providing a snapshot of a functioning microbial ecosystem in a terrestrial volcanic habitat. The  
559 sedimentary features indicate a shallow lacustrine setting and deposition in a narrow-closed  
560 system with negligible stream and riverine input, recharged being most likely by hydrothermal

561 inflows and seasonal runoff. The development and preservation of putative microbial structures  
562 that flourished during short intervals of non-volcanic activity and suitable taphonomic  
563 conditions, including early lithification, provide strong support for the volcanic environment in  
564 which the mats grew, while at the same time constraining the taphonomic conditions that  
565 enabled the remarkable preservation of these alkaline lake biota, including features pointing to  
566 oxygenic photosynthesis.

567 The fossilized aggregates, the biogenic origin of the associated facies, silicification, the  
568 presence of EPS, and their Ediacaran age, lead us to propose the aggregates as either bacterial  
569 microcolonies or silica mineralized cell aggregates. See for example Xiao, Li, & Reynolds  
570 (2018) for a comparison. The data further demonstrate that the 571 Myr old Ediacaran Amane  
571 Tazgart alkaline lake supported a unique and diverse community of extremophiles specialized  
572 to thrive in equally unique high alkalinity terrestrial aquatic ecosystems. Particularly, the  
573 combined observation of geological indicators for oxygen production, with sedimentary  
574 abundance of stromatolites and their remarkably well-preserved gas escape structures and  
575 bubbles, highlight the radiation and spread of alkaliphilic oxygenic photosynthesizers to  
576 extreme alkaline environments since Ediacaran time. These organisms certainly contributed  
577 towards the oxygenation of their terrestrial lake ecosystem habitats, raising fundamental  
578 questions about the contribution of the terrestrial biosphere to Precambrian atmospheric  
579 oxygenation and to early nutrient biogeochemical cycles.

580

581

582 **Figure captions**

583 **Figure 1** (a) Geological map of the Anti-atlas of Morocco. (b) Structural Map of Oued Dar´a  
584 caldera. (c) Geological Map of Amane Tazgart´s microbialites. (d) Geological cross-section of  
585 Amane Tazgart site.

586

587 **Figure 2** Detailed lithostratigraphic column of the Amane Tazgart biofacies. Chlorite (Chl),  
588 Illite (Il), mixed-layer minerals (MLM) and chlorite/smectite (C/S), represent the Clay  
589 mineralogical assemblages of the various microbialitic facies.

590

591 **Figure 3** (a) Thrombolitic facies with irregular to patchy shaped mesoclots. (b) Polished slab  
592 of (a). Mesoclots (Ms). Silicified matrix (Sm). (c) Thin-section photomicrograph of  
593 thrombolites (Cm= clotted micrite, Ce= botryoidal calcite cement). (d) Thin-section  
594 photomicrograph of laminated mesoclots constituted with alternate light sparitic and peloidal  
595 micritic laminae. (e) Thin-section photomicrograph of laminated matrix in thrombolites. (f)  
596 Field view of composite microbial structure between thrombolites (Cl=clotted fabric) and  
597 stromatolites (Lm=laminated fabric). (g) Polished slab from same sample as panel f. (h) Thin-  
598 section photomicrograph of a composite microbial structure showing mesoclots (Cl) draped by  
599 a laminated fabric (Lm). (i) Thin-section photomicrograph of the laminated fabrics in  
600 composites microbialites constituted of alternating grain-sized (Gs), sparitic (Sp), and micritic  
601 laminae (Mi). (j-k) Flat to large domal carbonate stromatolites. (l) Thin-section  
602 photomicrograph of flat to large domal stromatolites showing wavy-crinkly aspects between  
603 iron crusts micritic laminae (Mi) and sparites (Sp). The white arrow shows tufted microbial  
604 mats. The coin is 2.4 cm in diameter.

605

606 **Figure 4** (a) Laminated to pseudo-columnar stromatolites. (b) Stromatolitic dome, (c) cones.  
607 (d) vertical columns, (e) tilted columns. (f) composite dome with laminations first developing  
608 in circular patterns in the axial part of the column before transitioning to progressively wavier  
609 architecture towards the margins. (g) Thin-section photomicrograph of alternating grain-sized  
610 (Gl) and iron rich laminae (Ir). (h) Thin-section photomicrograph of alternating micritic (Mi)  
611 and sparitic laminae (Sp). (i) Thin-section photomicrograph of a peloidal to clotted micritic  
612 laminae. (j) Thin-section photomicrograph of fossilized gas bubble structure (yellow arrow).  
613 (k) Thin-section photomicrograph of composite alternate type laminae between light sparitic  
614 and dark wrinkled-crinkled grain-sized laminae. (l) Thin-section photomicrograph of repetitive  
615 style laminae. Pen is 15 cm long. The coin is 2.4 cm in diameter.

616

617 **Figure 5** (a) Polished slab of flat pebble calcirudite, (b) Polished slab of rounded shape  
618 microbial clasts in a calcirudite. (c) Polished slab of the spherulitic facies, showing spherulites  
619 (arrow) and microbial derived clasts=Mc. (d) Thin-section photomicrograph of spherulites  
620 embedded in an epiclastic sand-sized matrix, containing a spherical spherulite with a clastic  
621 nucleus, surrounded by coarse-grained wedge-shaped calcite crystals (1), and an oval spherulite  
622 (2) with a micrite-microspar core (dashed lines). (e) Rippled sandy calcarenites covered with  
623 stromatolitic layers. (f) Thin-section photomicrograph of the microbial lamination of (e)  
624 showing coarse-grained microbial mats, and wrinkly-crinkly iron rich laminae.

625 **Figure 6** (a) Ripple marks structures. (b) Domal sand buildups (arrows). (c) Crescent structures  
626 (dashed lines). (d) Thin-section photomicrograph of gas escape structure in a crescent shape  
627 structure. (e) Globular peperites superposed with fluidal elongated lava clasts (dash lines outline  
628 globular lava clasts). (f) Thin-section photomicrograph of a peperites showing the epiclastic  
629 nature of sediments=Sd, surrounding volcanic clasts=Vo. Pen is 15 cm long and coin 2.4 cm in  
630 diameter.

631

632 **Figure 7** (a) Bulk-rock X-ray diffraction patterns of thrombolites, (b) Bulk-rock X-ray  
633 diffraction patterns of a clastic deposit associated with thrombolites. (c) Bulk-rock X-ray  
634 diffraction patterns of clastic stromatolites. (d) Bulk-rock X-ray diffraction patterns of clastic  
635 sediments within stromatolites, Chlorite=C, Calcite=Ca, K- Felds=F, hematite=He, illite=I,  
636 plagioclase=P, quartz=Q). Red areas designate the highest peak of calcite minerals, while green  
637 areas indicate the apogee of quartz minerals.

638 **Figure 8** XRD diffractogram of air dried (1) ethylene-glycol solvation, (2) thermal treatment  
639 at 350°C, (3) et 550°C, (4) of microbialitic, and detritic samples. (a) XRD diffractogram of the  
640 microbialitic horizon H1 located at the base of the section showing a C/S MLM dominated by  
641 chlorite as indicated by a peak of 15 Å in ethylene-glycol treatment (red circle). (b) XRD  
642 diffractogram of detritic facies at the base of the section similar to observations in panel (a).  
643 (c)-(d) XRD diffractograms of a clastic sample from the last detritic interval (c) and from the  
644 last stromatolitic horizon (d) showing a superlattice reflections of 29-30 Å (red circles) that  
645 indicates a mixed layer mineral C/S MLM more enriched in smectite than chlorite in the upper  
646 part of the section. Minerals: calcite=Ca, chlorite=C, K-Feldspar=F, (I) Illite/Mica=MI, mixed  
647 layers chlorite/smectite, plagioclase=P, quartz=q.

648

649 **Figure 9** SEM images of aggregates extracted from the spherulites. (a-g) Spherical or globular  
650 morphologies. (h.l) Irregular morphologies.

651

652 **Figure 10** (a-b) SEM images of an example of preserved EPS sheets and joined aggregates  
653 (white arrows). (c) SEM image of globular aggregates preserving a sheet covering a portion of  
654 the aggregates (white square). (d) EDS analyses of the aggregates and the sheet reveal a silica-  
655 rich composition (green circle) containing some carbon (black circle) in the aggregates (Spot

656 1). The sheets contain considerable amounts of carbon relative to silica, and detectable  
657 proportions of sulfur, magnesium, chlorine and arsenic (Spot 2).

658

659 **Figure 11** (a) Details of aggregates showing coccoidal and coccobacilli-like crystals indicated  
660 by white arrows and related EDS analysis showing a predominantly silica-rich composition and  
661 some carbon. (b) Coccoidal bacterial-like molds embedded in calcite crystals indicated by white  
662 arrows. (c) Clay minerals in dark columnar stromatolitic Laminae. (d) 3D SEM  
663 photomicrograph of a 3D spherulitic samples composed primarily of radially arranged calcite  
664 crystals forming cortices and micritic circular nuclei marked by a dashed line (e=EDS analyses  
665 of nucleus showing a composition of calcite associated with clays containing Si, Al, K, and iron  
666 (Fe). (f)=EDS analysis suggests the cortices are composed mostly of pure calcite).

667

668 **References**

- 669 Adachi, N., Ezaki, Y., Liu, J., Watabe, M., Sonoda, H., Altanshagai, G., Enkhbaatar, B.  
670 Dorjnamjaa, D. (2019). Late Ediacaran Boxonia-bearing stromatolites from the Gobi-Altay,  
671 western Mongolia. *Precambrian Research*, 334, 105470.  
672 <https://doi.org/10.1016/j.precamres.2019.105470>
- 673 Altermann, W., Kazmierczak, J., Oren, A., & Wright, D. T. (2006). Cyanobacterial  
674 calcification and its rock-building potential during 3.5 billion years of Earth history.  
675 *Geobiology*, 4, 147–166. <https://doi.org/10.1111/j.1472-4669.2006.00076.x>
- 676 Álvaro, J. J., Ezzouhairi, H., Ait Ayad, N., Charif, A., Solá, R., & Ribeiro, M. L. (2010).  
677 Alkaline lake systems with stromatolitic shorelines in the Ediacaran volcanosedimentary  
678 Ouarzazate Supergroup, Anti-Atlas, Morocco. *Precambrian Research*, 179(1–4), 22–36.  
679 <https://doi.org/10.1016/j.precamres.2010.02.009>
- 680 Álvaro, J. J., & González-Acebrón, L. (2019). Sublacustrine hydrothermal seeps and  
681 silicification of microbial bioherms in the Ediacaran Oued Dar'a caldera, Anti-Atlas,  
682 Morocco. *Sedimentology*, (ii). <https://doi.org/10.1111/sed.12568>
- 683 Andres, M. S., & Pamela Reid, R. (2006). Growth morphologies of modern marine  
684 stromatolites: A case study from Highborne Cay, Bahamas. *Sedimentary Geology*, 185(3–4),  
685 319–328. <https://doi.org/10.1016/J.SEDGEO.2005.12.020>
- 686 Arp, G., Helms, G., Karlinska, K., Schumann, G., Reimer, A., Reitner, J., & Trichet, J.  
687 (2012). Photosynthesis versus Exopolymer Degradation in the Formation of Microbialites on  
688 the Atoll of Kiritimati, Republic of Kiribati, Central Pacific. *Geomicrobiology Journal*, 29(1),  
689 29–65. <https://doi.org/10.1080/01490451.2010.521436>

690 Aubineau, J., El Albani, A., Bekker, A., Somogyi, A., Bankole, O. M., Macchiarelli, R.,  
691 Meunier, A., Riboulleau, A., Reynaud, J., Konhauser, K. O. (2019). Microbially induced  
692 potassium enrichment in Paleoproterozoic shales and implications for reverse weathering on  
693 early Earth. *Nature Communications*, 10(1), 2670. [https://doi.org/10.1038/s41467-019-10620-](https://doi.org/10.1038/s41467-019-10620-3)  
694 3

695 Banerjee, S., Sarkar, S., Eriksson, P. G., & Samanta, P. (2010). Microbially Related  
696 Structures in Siliciclastic Sediment Resembling Ediacaran Fossils: Examples from India,  
697 Ancient and Modern. *Geobiology*, 109–129. [https://doi.org/10.1007/978-90-481-3799-2\\_6](https://doi.org/10.1007/978-90-481-3799-2_6)

698 Bosak, T., Bush, J. W. M., Flynn, M. R., Liang, B., Ono, S., Petroff, A. P., & Sim, M. S.  
699 (2010). Formation and stability of oxygen-rich bubbles that shape photosynthetic mats.  
700 *Geobiology*, 8(1), 45-55. <https://doi.org/10.1111/j.1472-4669.2009.00227.x>

701 Bosak, Tanja, Knoll, A. H., & Petroff, A. P. (2013). The Meaning of Stromatolites. *Annual*  
702 *Review of Earth and Planetary Sciences*, 41(1), 21–44. [https://doi.org/10.1146/annurev-earth-](https://doi.org/10.1146/annurev-earth-042711-105327)  
703 042711-105327

704 Bosak, Tanja, Liang, B., Min, S. S., & Petroff, A. P. (2009). Morphological record of  
705 oxygenic photosynthesis in conical stromatolites. *Proceedings of the National Academy of*  
706 *Sciences of the United States of America*, 106(27), 10939–10943.  
707 <https://doi.org/10.1073/pnas.0900885106>

708 Bottjer, D., & Hagadorn, J. W. (2007). Mat growth features. *Atlas of Microbial Mat Features*  
709 *Preserved Within the Clastic Rock Record*. Elsevier, Amsterdam, New York, 53-71. Bouton,  
710 A., Vennin, E., Pace, A., Bourillot, R., Dupraz, C., Thomazo, C., Brayard, A., Désaubliaux,  
711 G., Visscher, P. T. (2016). External controls on the distribution, fabrics and mineralization of  
712 modern microbial mats in a coastal hypersaline lagoon, Cayo Coco (Cuba). *Sedimentology*,  
713 63(4), 972–1016. <https://doi.org/10.1111/sed.12246>

714 Chagas, A. A. P., Webb, G. E., Burne, R. V., & Southam, G. (2016). Modern lacustrine  
715 microbialites: Towards a synthesis of aqueous and carbonate geochemistry and mineralogy.  
716 *Earth-Science Reviews*, 162, 338–363. <https://doi.org/10.1016/j.earscirev.2016.09.012>

717 Chafetz, H., Barth, J., Cook, M., Guo, X., & Zhou, J. (2018). Origins of carbonate spherulites:  
718 implications for Brazilian Aptian pre-salt reservoir. *Sedimentary Geology*, 365, 21-33.  
719 <https://doi.org/10.1016/j.sedgeo.2017.12.024>

720 Chi Fru, E., Arvestål, E., Callac, N., El Albani, A., Kiliyas, S., Argyraki, A., & Jakobsson, M.  
721 (2015). Arsenic stress after the Proterozoic glaciations. *Scientific Reports*, 5, 17789.  
722 <https://doi.org/10.1038/srep17789>

723 Chi Fru, E., Callac, N., Posth, N. R., Argyraki, A., Ling, Y. C., Ivarsson, M., Broman, C.,  
724 Kiliyas, S. P. (2018). Arsenic and high affinity phosphate uptake gene distribution in shallow  
725 submarine hydrothermal sediments. *Biogeochemistry*, 141(1), 41–62.  
726 <https://doi.org/10.1007/s10533-018-0500-8>

727 Choubert, G., Faure-Muret, A. (1970). Les corrélations du Précambrien, Anti-Atlas occidental  
728 et central. Colloque international sur les corrélations du Précambrien: Agadir – Rabat, 3–23  
729 mai 1970. Livret guide de l'excursion : Anti-Atlas occidental et central. *Notes et Mémoires*  
730 *Du Service Géologique Du Maroc*, 229, 259.

731 Dongjie, T., Xiaoying, S., Ganqing, J., Yunpeng, P., Wenhao, Z., Yuan, W., & Min, L.  
732 (2013). Environment controls on Mesoproterozoic thrombolite morphogenesis: A case study  
733 from the North China Platform. *Journal of Palaeogeography*, 2(3), 275–296.

734 Dupraz, C., & Visscher, P. T. (2005). Microbial lithification in marine stromatolites and  
735 hypersaline mats. *Trends in Microbiology*, 13(9), 429–438.  
736 <https://doi.org/10.1016/J.TIM.2005.07.008>

737 Eymard, I., Alvarez, M. del P., Bilmes, A., Vasconcelos, C., & Ariztegui, D. (2020). Tracking  
738 Organomineralization Processes from Living Microbial Mats to Fossil Microbialites.  
739 *Minerals*, 10(7), 605. <https://doi.org/10.3390/min10070605>

740 Gerdes, G. (2010). What are Microbial Mats? [https://doi.org/10.1007/978-90-481-3799-2\\_1](https://doi.org/10.1007/978-90-481-3799-2_1)

741 Gerdes, G., Klenke, T., & Noffke, N. (2000). Microbial signatures in peritidal siliciclastic  
742 sediments: A catalogue. *Sedimentology*, 47(2), 279–308. <https://doi.org/10.1046/j.1365-3091.2000.00284.x>

743

744 Harwood, C. L., & Sumner, D. Y. (2011). Microbialites of the Neoproterozoic Beck Spring  
745 Dolomite, Southern California. *Sedimentology*, 58(6), 1648–1673.  
746 <https://doi.org/10.1111/j.1365-3091.2011.01228.x>

747 Hickman-Lewis, K., Cavalazzi, B., Foucher, F., & Westall, F. (2018). Most ancient evidence  
748 for life in the Barberton greenstone belt: Microbial mats and biofabrics of the ~3.47 Ga  
749 Middle Marker horizon. *Precambrian Research*, 312, 45–67.  
750 <https://doi.org/10.1016/j.precamres.2018.04.007>

751 Kaźmierczak, J., Kempe, S., Kremer, B., López-García, P., Moreira, D., & Tavera, R. (2011).  
752 Hydrochemistry and microbialites of the alkaline crater lake Alchichica, Mexico. *Facies*,  
753 57(4), 543–570. <https://doi.org/10.1007/s10347-010-0255-8>

754 Kirkham, A., & Tucker, M. E. (2018). Thrombolites, spherulites and fibrous crusts  
755 (Holkerian, Purbeckian, Aptian): Context, fabrics and origins. *Sedimentary Geology*, 374, 69–  
756 84. <https://doi.org/10.1016/j.sedgeo.2018.07.002>

757 Knoll, A. H., Bergmann, K. D., & Strauss, J. V. (2016,). Life: The first two billion years.  
758 *Philosophical Transactions of the Royal Society B: Biological Sciences*, Vol. 371 (1707),  
759 20150493. <https://doi.org/10.1098/rstb.2015.0493>

760 Kremer, B., Kaźmierczak, J., & Kempe, S. (2019). Authigenic replacement of  
761 cyanobacterially precipitated calcium carbonate by aluminium-silicates in giant microbialites  
762 of Lake Van (Turkey). *Sedimentology*, 66(1), 285–304. <https://doi.org/10.1111/sed.12529>

763 Kulp, T. R., Hoeft, S. E., Asao, M., Madigan, M. T., Hollibaugh, J. T., Fisher, J. C., Stolz, J.  
764 F., Culbertson, C. W., Miller, L. G., Oremland, R. S. (2008). Arsenic(III) fuels anoxygenic  
765 photosynthesis in hot spring biofilms from Mono Lake, California. *Science*, 321(5891), 967–  
766 970. <https://doi.org/10.1126/science.1160799>

767 McCann Hoeft, S., Boren, A., Hernandez-Maldonado, J., Stoneburner, B., Saltikov, C., Stolz,  
768 J., & Oremland, R. (2016). Arsenite as an Electron Donor for Anoxygenic Photosynthesis:  
769 Description of Three Strains of Ectothiorhodospira from Mono Lake, California and Big Soda  
770 Lake, Nevada. *Life*, 7(1), 1. <https://doi.org/10.3390/life7010001>

771 Mercedes-Martín, R., Rogerson, M. R., Brasier, A. T., Vonhof, H. B., Prior, T. J., Fellows, S.  
772 M., Reijmer, J.J.G. Billing, I. Pedley, H. M. (2016). Growing spherulitic calcite grains in  
773 saline, hyperalkaline lakes: experimental evaluation of the effects of Mg-clays and organic  
774 acids. *Sedimentary Geology*, 335, 93–102. 335, 93–102.  
775 <https://doi.org/10.1016/J.SEDGEO.2016.02.008>

776 Merino, N., Aronson, H. S., Bojanova, D. P., Feyhl-Buska, J., Wong, M. L., Zhang, S., &  
777 Giovannelli, D. (2019). Living at the extremes: Extremophiles and the limits of life in a  
778 planetary context. *Frontiers in Microbiology*, 10, 780.  
779 <https://doi.org/10.3389/fmicb.2019.00780>

780 Monty, C. L. V. (1976). The Origin and Development of Cryptalgal Fabrics. *Developments in*  
781 *Sedimentology*, 20, 193–249. [https://doi.org/10.1016/S0070-4571\(08\)71137-3](https://doi.org/10.1016/S0070-4571(08)71137-3)

782 Moore, D. M., & Reynolds Jr, R. C. (1989). X-ray Diffraction and the Identification and  
783 Analysis of Clay Minerals. Oxford University Press (OUP).

784 Noffke, N., & Awramik, S. M. (2013). Stromatolites and MISS-Differences between relatives.  
785 GSA Today, 23(9), 4–9. <https://doi.org/10.1130/GSATG187A.1>

786 Pecoraino, G., & Alessandro, W. D. (2015). The Other Side of the Coin: Geochemistry of  
787 Alkaline Lakes in Volcanic Areas. *Volcanic lakes*, 219-237. [https://doi.org/10.1007/978-3-](https://doi.org/10.1007/978-3-642-36833-2)  
788 [642-36833-2](https://doi.org/10.1007/978-3-642-36833-2)

789 Perri, E., Tucker, M. E., Słowakiewicz, M., Whitaker, F., Bowen, L., & Perrotta, I. D. (2018).  
790 Carbonate and silicate biomineralization in a hypersaline microbial mat (Mesaieed sabkha,  
791 Qatar): Roles of bacteria, extracellular polymeric substances and viruses. *Sedimentology*,  
792 65(4), 1213–1245. <https://doi.org/10.1111/sed.12419>

793 Planavsky, N., & Grey, K. (2008). Stromatolite branching in the Neoproterozoic of the  
794 Centralian Superbasin, Australia: an investigation into sedimentary and microbial control of  
795 stromatolite morphology. *Geobiology*, 6(1), 33-45. [https://doi.org/10.1111/j.1472-](https://doi.org/10.1111/j.1472-4669.2007.00116.x)  
796 [4669.2007.00116.x](https://doi.org/10.1111/j.1472-4669.2007.00116.x)

797 Reid, R. P., James, N. P., Macintyre, I. G., Dupraz, C. P., & Burne, R. V. (2003). Shark Bay  
798 stromatolites: Microfabrics and reinterpretation of origins. *Facies*, 49(1), 299.  
799 <https://doi.org/10.1007/s10347-003-0036-8>

800 Riding, R. (1991). Classification of Microbial Carbonates. *Calcareous Algae and*  
801 *Stromatolites*. 21–51. [https://doi.org/10.1007/978-3-642-52335-9\\_2](https://doi.org/10.1007/978-3-642-52335-9_2)

802 Riding, R. (2011). Microbialites, stromatolites, and thrombolites. *Encyclopedia of geobiology*.  
803 <https://doi.org/10.1007/978-1-4020-9212-1>

804 Sallstedt, T., Bengtson, S., Broman, C., Crill, P. M., & Canfield, D. E. (2018). Evidence of  
805 oxygenic phototrophy in ancient phosphatic stromatolites from the Paleoproterozoic  
806 Vindhyan and Aravalli Supergroups, India. *Geobiology*, 16(2), 139–159.  
807 <https://doi.org/10.1111/gbi.12274>

808 Sancho-Tomás, M., Somogyi, A., Medjoubi, K., Bergamaschi, A., Visscher, P.T., Van  
809 Driessche A.E.S., Gérard, E., Farias, M.E., Contreras, M., Philippot, P. (2018). Distribution,  
810 redox state and (bio)geochemical implications of arsenic in present day microbialites of  
811 Laguna Brava, Salar de Atacama. *Chemical. Geology*. 490, 13–21.  
812 <https://doi.org/10.1016/j.chemgeo.2018.04.029>

813 Sanz-Montero, M. E., Cabestrero, Ó., & Sánchez-Román, M. (2019). Microbial Mg-rich  
814 Carbonates in an Extreme Alkaline Lake (Las Eras, Central Spain). *Frontiers in*  
815 *Microbiology*, 10, 148. <https://doi.org/10.3389/fmicb.2019.00148>

816 Schagerl, M., & Burian, A. (2016). The ecology of African soda lakes: driven by variable and  
817 extreme conditions. *Soda Lakes of East Africa*. 12, 295–320. [https://doi.org/10.1007/978-3-](https://doi.org/10.1007/978-3-319-28622-8)  
818 [319-28622-8](https://doi.org/10.1007/978-3-319-28622-8)

819 Sforza, M.C., Daye, M., Philippot, P., Somogyi, A., van Zuilen, M.A., Medjoubi, K., Gérard, E.,  
820 Jamme, F., Dupraz, C., Braissant, O., Glunk, C., & Visscher, P.T. (2017). Patterns of metal  
821 distribution in hypersaline microbialites during early diagenesis: implications for the fossil  
822 record. *Geobiology*, 15(2), 259–279. <https://doi.org/10.1111/gbi.12218>

823 Sforza, M. C., Philippot, P., Somogyi, A., Van Zuilen, M. A., Medjoubi, K., Schoepp-Cothenet,  
824 B., Nitshke, W., Visscher, P. T. (2014). Evidence for arsenic metabolism and cycling by  
825 microorganisms 2.7 billion years ago. *Nature Geoscience*, 7, 811–815.  
826 <https://doi.org/10.1038/ngeo2276>

827 Sheng, G.-P., Yu, H.-Q., & Li, X.-Y. (2010). Extracellular polymeric substances (EPS) of  
828 microbial aggregates in biological wastewater treatment systems: A review. *Biotechnology  
829 Advances*, 28(6), 882–894. <https://doi.org/10.1016/J.BIOTECHADV.2010.08.001>

830 Skilling, I. P., White, J. D. L., & McPhie, J. (2002). Peperites: A review of magma-sediment  
831 mingling. *Journal of Volcanology and Geothermal Research*, 114(1–2), 1–17.  
832 [https://doi.org/10.1016/S0377-0273\(01\)00278-5](https://doi.org/10.1016/S0377-0273(01)00278-5)

833 Środoń, J. (1999). Nature of Mixed-Layer Clays and Mechanisms of Their Formation and  
834 Alteration. *Annual Review of Earth and Planetary Sciences*, 27(1), 19–53.  
835 <https://doi.org/10.1146/annurev.earth.27.1.19>

836 Stüeken, Eva E., & Buick, R. (2018). Environmental control on microbial diversification and  
837 methane production in the Mesoarchean. *Precambrian Research*, 304, 64–72.  
838 <https://doi.org/10.1016/j.precamres.2017.11.003>

839 Suarez-Gonzalez, P., Benito, M. I., Quijada, I. E., Mas, R., & Campos-Soto, S. (2019).  
840 ‘Trapping and binding’: A review of the factors controlling the development of fossil  
841 agglutinated microbialites and their distribution in space and time. *Earth-Science Reviews*,  
842 194, 182-215. <https://doi.org/10.1016/j.earscirev.2019.05.007>

843 Sumner, D. Y., Hawes, I., Mackey, T. J., Jungblut, A. D., & Doran, P. T. (2015). Antarctic  
844 microbial mats: A modern analog for Archean lacustrine oxygen oases. *Geology*, 43(10), 887–  
845 890. <https://doi.org/10.1130/G36966.1>

846 Tang, D., Shi, X., & Jiang, G. (2013). Mesoproterozoic biogenic thrombolites from the North  
847 China platform. *International Journal of Earth Sciences*, 102(2), 401–413.  
848 <https://doi.org/10.1007/s00531-012-0817-9>

849 Thomas, R. J., Chevallier, L. P., Gresse, P. G., Harmer, R. E., Eglinton, B. M., Armstrong,  
850 R. A., De Beer, C. H., Martini, J. E. J., De Kock, G. S., Macey, P. H., Ingram, B. A. (2002).  
851 Precambrian evolution of the Sirwa Window, Anti-Atlas Orogen, Morocco. *Precambrian*  
852 *Research*, 118(1–2), 1–57. [https://doi.org/10.1016/S0301-9268\(02\)00075-X](https://doi.org/10.1016/S0301-9268(02)00075-X)

853 Thomas, R. J., Fekkak, A., Ennih, N., Errami, E., & Loughlin, S. C. (2004). A new  
854 lithostratigraphic framework for the Anti-Atlas Orogen, Morocco. *Journal of African Earth*  
855 *Sciences*, 39(3-5), 217-226. <https://doi.org/10.1016/j.jafrearsci.2004.07.046>

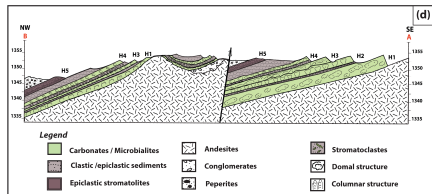
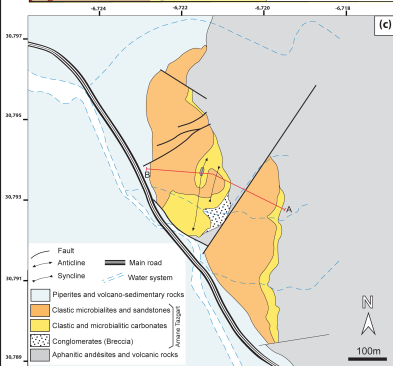
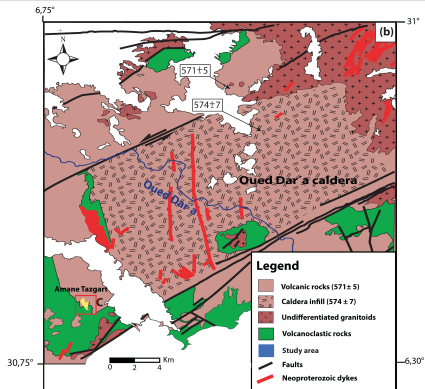
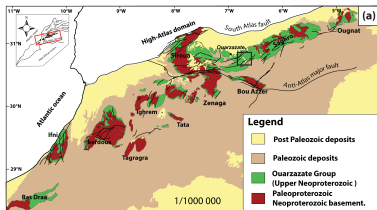
856 Tuduri, J., Chauvet, A., Barbanson, L., Bourdier, J., Labriki, M., Ennaciri, A., Badra, L.,  
857 Dubois, M., Ennaciri-leloix, C., Sizaret, S., Maacha, L. (2018). The Jbel Saghro Au (– Ag ,  
858 Cu ) and Ag – Hg Metallogenic Province : Product of a Long-Lived Ediacaran Tectono-  
859 Magmatic Evolution in the Moroccan Anti-Atlas. *Minerals*, 8(12), 592.  
860 <https://doi.org/10.3390/min8120592>

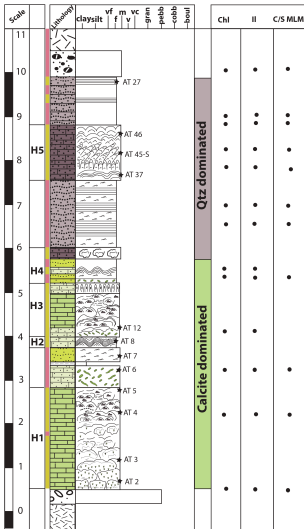
861 Van Kranendonk, M. J., Djokic, T., Poole, G., Tadbiri, S., Steller, L., & Baumgartner, R.  
862 (2019). Depositional Setting of the Fossiliferous, c.3480 Ma Dresser Formation, Pilbara  
863 Craton. *Earth's Oldest Rocks*, 985–1006. [https://doi.org/10.1016/b978-0-444-63901-](https://doi.org/10.1016/b978-0-444-63901-1.00040-x)  
864 [1.00040-x](https://doi.org/10.1016/b978-0-444-63901-1.00040-x)

865 Walsh, G. J., Benziane, F., Aleinikoff, J. N., Harrison, R. W., Yazidi, A., Burton, W. C.,  
866 Quick, J. E., Saadane, A. (2012). Neoproterozoic tectonic evolution of the Jebel Saghro and  
867 Bou Azzer—El Graara inliers, eastern and central Anti-Atlas, Morocco. *Precambrian*  
868 *Research*, 216–219, 23–62. <https://doi.org/10.1016/J.PRECAMRES.2012.06.010>

869 Willmer, P., Stone, G., & Johnston, I. (2004). *Environmental Physiology of Animals* (2nd  
870 ed.).

- 871 Wright, V. P., & Barnett, A. J. (2015). An abiotic model for the development of textures in  
872 some South Atlantic early Cretaceous lacustrine carbonates. *Geological Society Special*  
873 *Publication*, 418(1), 209–219. <https://doi.org/10.1144/SP418.3>
- 874 Xiao, M., Li, M., & Reynolds, C. S. (2018). Colony formation in the cyanobacterium  
875 *Microcystis*. *Biological Reviews*, 93(3), 1399–1420. <https://doi.org/10.1111/brv.12401>





## Legende

### Facies

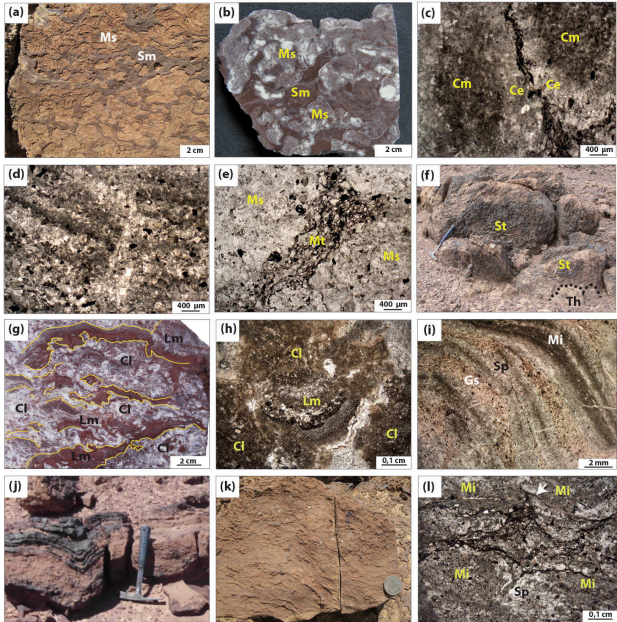
-  Carbonate
-  Sandy limestones
-  Calcarenites
-  Sandstones
-  Clastic stromatolites
-  Silty sands
-  Conglomerates
-  Peperites
-  Andesites
-  Microbialite-derived clasts

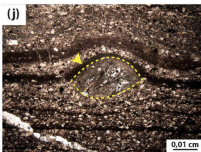
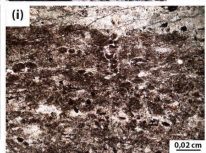
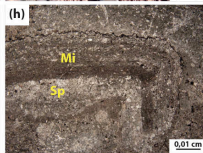
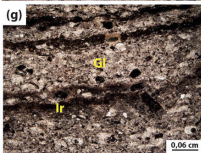
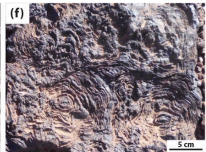
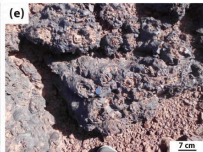
### Sedimentary structures

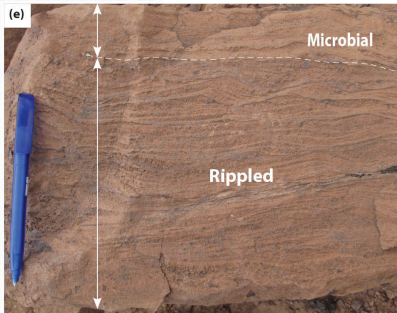
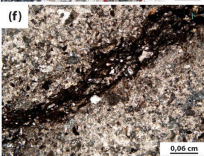
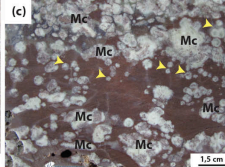
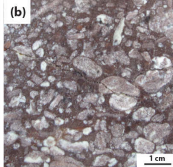
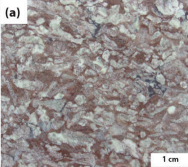
-  Ripple bedding
-  Planar laminated
-  Composite microbialites
-  Domal structure
-  Flat domal stromatolites
-  Columnar stromatolites
-  Spherulites

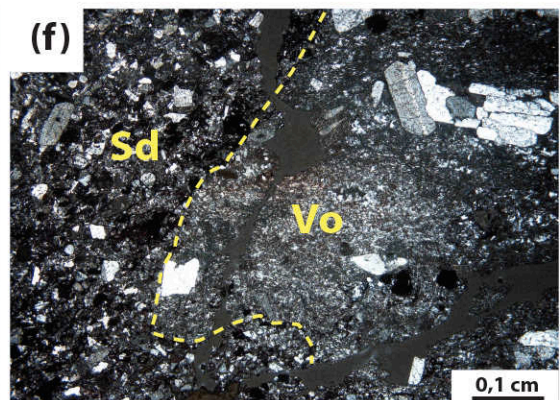
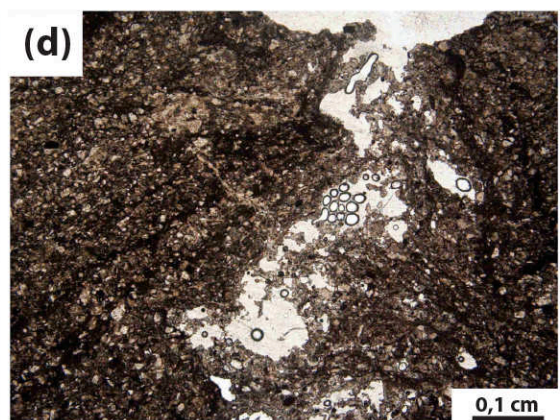
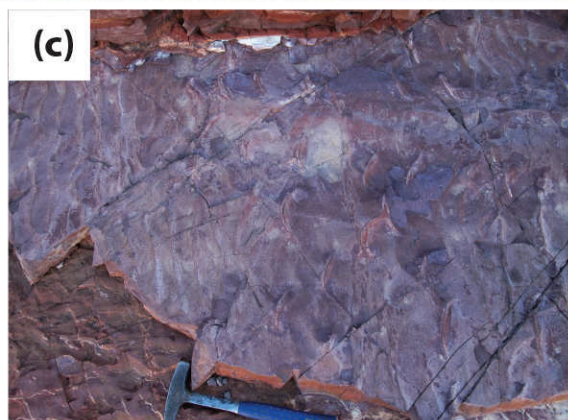
### Facies type

-  Microbial origin
-  Physical origin

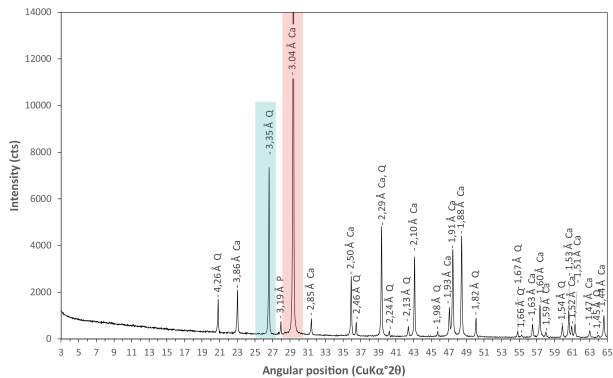




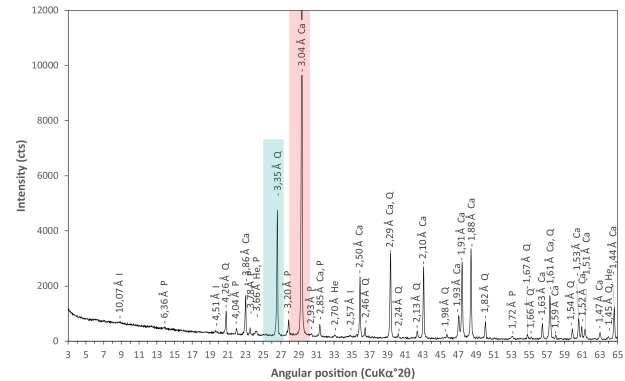




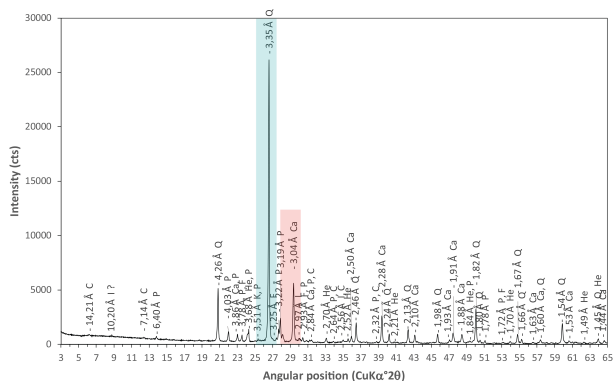
(a)



(b)



(c)



(d)

